Journal of Catalysis **210,** 405–417 (2002)
doi:10.1006/jcat.2002.3712

Cu–Co Synergism in $Cu_{1-x}Co_xFe_2O_4$—Catalysis and XPS Aspects

Thomas Mathew, N. R. Shiju, K. Sreekumar, Bollapragada S. Rao, and Chinnakonda S. Gopinath[1]

Catalysis Division, National Chemical Laboratory, Dr. Homi Bhabha Road, Pune 411 008, India

Received February 25, 2002; revised May 24, 2002; accepted June 5, 2002

A systematic study on catalytic methylation of phenol is carried out with methanol as a function of reaction temperature and catalyst composition on a $Cu_{1-x}Co_xFe_2O_4$ ($x = 0.0$ to 1.0) ferrospinel system. Phenol methylation gives two major products, namely *o*-cresol and 2,6-xylenol. Large phenol conversion and 2,6-xylenol production are observed at 350°C and $x = 0.5$ shows good catalytic performance. Increase in selectivity of 2,6-xylenol at the expense of *o*-cresol demonstrates that the phenol methylation is sequential. X-ray diffraction of fresh catalysts reveals the formation of the spinel phase along with a mixture of CuO and α-Fe_2O_3 phases at $x = 0.0$, while trace amounts of α-Fe_2O_3 are found for $x \geq 0.25$. Spent catalysts display better crystallinity, hinting at the integrity of the structure. X-ray photoelectron spectroscopy and X-ray-induced Auger electron spectroscopy reveal the presence of Cu^{2+}, Fe^{3+}, Co^{2+}, and Co^{3+} species on fresh catalysts. Metal ions reduce partially to lower oxidation states on spent catalysts. Reducibility of Cu^{2+} species decreases with increasing x. Valence band photoemission studies demonstrate a clear change in the overlap between 3d bands of Cu, Co, and Fe from fresh to spent catalysts. The better catalytic results observed with $x = 0.5$ are attributed to an optimum distribution of Cu species with heteroatom neighbors on the surface, and the maximum overlap between the Cu and Co 3d bands makes the ferrospinel integrate chemically and electronically.

Key Words: **ferrospinel; $Cu_{1-x}Co_xFe_2O_4$; phenol methylation; *o*-cresol; 2,6-xylenol; XPS; XAES; Cu–Co synergism; carbon hydrogenation.**

1. INTRODUCTION

Among the various catalysts used for aromatic alkylation, metal oxides and spinel (AB_2O_4) compounds have been effective and the above systems have been characterized well (1–28). Inverse spinel systems $B(AB)O_4$ are more interesting due to the versatile nature of cation distribution in tetrahedral (T_d) and octahedral (O_h) sites. Our earlier work on aromatic ring methylation of pyridine, N-alkylation of aniline with $(Zn/Ni)_{1-x}Co_xFe_2O_4$ (26–28), and phenol methylation with $CuFe_2O_4$ and $CoFe_2O_4$ (29, 30) revealed the catalytic effectiveness of ferrospinels and the possibility of tuning the catalyst composition toward any specific alkylation reaction. Robust structural features of the ferrospinels enable them to withstand a harsh reducing atmosphere even under the reduction of Fe^{3+} to Fe^{2+} (31) and the original state can be regained by simple oxidation. This demonstrates that Fe^{3+} can be shunted between T_d and O_h sites by varying the concentration of other cations. This leads to changes in acid–base properties and cation distribution of the spinel lattice and hence in catalytic activity and product selectivity. Although there have been few reports on the catalytic activity of the above system for different reactions, there have not been, to the best of our knowledge, any detailed studies on the selective *ortho* methylation of phenol, electronic structure, and surface science studies of the catalysts and any correlation between them. The present paper deals with the above aspects and is part of a continuing study in our laboratory to understand the catalytic activity related to Cu–Co-based systems and ferrospinels (26–30, 32).

Alkylated phenols such as *o*-cresol and 2,6-xylenol are industrially important chemicals, as they are used extensively as intermediates in agrochemical and polymer industries (29, 30). A glance at the literature indicates the wide spectrum of catalysts employed for phenol alkylation reaction, ranging from metal oxides such as MgO, Fe_2O_3 (3–9, 14–21), and hydrotalcites (12, 13) to acidic zeolites such as H-ZSM-5 and HY (7, 8, 10, 11). However, the above catalysts are associated with either lack of reproducibility (due to lack of identification of the active phase) or high operative temperature and competitive formation of anisole and *meta*- and *para*-alkylated products. Fe_2O_3 systems for phenol methylation demonstrated that magnetite (Fe_3O_4) is the active phase. The overall methylation activity varies in the order $Fe_3O_4 < CoFe_2O_4 < CuFe_2O_4$ (29, 30), and Fe_3O_4 deactivates fast with the above-mentioned side products (17). The above fact indicates the larger role of divalent (A) ions in increasing the methylation rate. It is believed that, in general, mixed metal oxides bring out a synergetic behavior, well known among transition metal oxides, and enhances the catalytic activity (22–24). For example, Cu–Co multicomponent mixed oxide catalysts with supports, like ZnO, ZrO_2, and Al_2O_3, are being used in important processes such as methanol reforming as well as in

[1] To whom correspondence should be addressed. E-mail: gopi@cata.ncl.res.in.

0021-9517/02 $35.00

low-pressure methanol synthesis from syngas and indicates the importance of Cu–Co synergism (32–36).

In this work we prepared a series of ferrospinels containing Co and Cu, having the general formula $Cu_{1-x}Co_xFe_2O_4$ ($x = 0$ to 1), by adopting a soft chemical route and studied the catalytic methylation of phenol with methanol by means of vapor-phase reaction. Cu–Co interaction in the $Cu_{1-x}Co_xFe_2O_4$ spinel system is demonstrated through changes in the oxidation state and overlap of 3d bands of transition metal ions. Synergetic interaction of Cu and Co in the spinel system is useful for understanding the methylation of phenol and exploring its role in the catalytic activity of various reactions. It is also to be emphasized here that the Cu–Co mixed system can act as a dual reaction catalyst depending on the material preparation and reaction conditions, as indicated above.

2. EXPERIMENTAL

2.1. Synthesis and Characterization of $Cu_{1-x}Co_xFe_2O_4$ Spinel System

The ferrospinel system having the general formula $Cu_{1-x}Co_xFe_2O_4$ ($x = 0$, 0.25, 0.5, 0.75, and 1) was prepared by a coprecipitation technique, as described in our earlier publications (26–30). Briefly, AR-grade chemicals supplied by Qualigens chemicals were used as supplied, without further purification. Stoichiometric amounts of premixed metal nitrate solutions were added to NaOH solution under continuous stirring. The final pH of the resulting solution was adjusted to between 9.5 and 10. The precipitate was washed with demineralized water until Na^+ and NO_3^- ions disappeared. The precipitates were filtered and dried at 80°C in an air oven for about 36 h. The dried materials were powdered and calcined at 500°C.

The chemical compositions of calcined (fresh) catalysts were determined by X-ray fluorescence (XRF) spectroscopy. X-ray diffraction (XRD) patterns of the powder catalysts were recorded using a Rigaku Geigerflex instrument equipped with CuK_α radiation ($\lambda = 1.5405$ Å) with a Ni filter to verify the phase purity and to obtain the unit cell parameter (a) and crystallite size. The BET surface area and pore volume (V_p) of the catalysts were determined by a N_2 adsorption–desorption method at liquid N_2 temperature using a Quantachrome NOVA-1200 adsorption unit. All the above characterization results are given in Table 1.

X-ray photoelectron spectra (XPS) were acquired on a VG Microtech Multilab ESCA 3000 spectrometer using a nonmonochromatized Mg$K\alpha$ X-ray source ($h\nu = 1253.6$ eV) on *in situ* scraped fresh catalyst pellets and powder samples of spent catalysts. Selected spectra were recorded with Al$K\alpha$ X-ray ($h\nu = 1486.6$ eV) also to eliminate the overlap between different Auger and core levels. Base pressure in the analysis chamber was maintained in the range of $3–6 \times 10^{-10}$ torr. Energy resolution of the spectrometer was set at 0.8 (1.1) eV with Mg$K\alpha$ (Al$K\alpha$) radiation at a pass energy of 20 eV. The error in the BE values reported is ±0.1 eV. More details about the instrument are available in our earlier work (37, 38).

2.2. Catalytic Activity Measurements

Vapor-phase alkylation of phenol with methanol was performed at atmospheric pressure in a fixed-bed, vertical, down-flow, integral silica reactor placed inside a double-zone furnace (Geomechanique, France). Three grams of fresh catalyst with a particle size up to 20 mesh was charged each time in the center of the reactor in such a way that the catalyst was sandwiched between the layers of inert porcelain beads. The upper portion of the reactor served as a vaporizer cum preheater. A thermocouple was positioned at the center of the catalyst bed to monitor the exact temperature of the catalyst. The reactant mixture was fed by a syringe pump (ISCO, Model 500D) at a weight hourly space velocity (WHSV) of 0.869 h^{-1} for all the measurements reported in this paper. Reaction products were analyzed and characterized by GC, GC–MS, and GC–IR. It is evident from the following discussion that several factors contribute to the total catalytic activity at different extents. In addition, the difficulty in determining the specific surface

TABLE 1

Chemical Analysis, XRD Parameters, and Surface Area of $Cu_{1-x}Co_xFe_2O_4$

Catalyst composition (x)	Metal concentration (wt%)[a]			Crystallite size (nm)[b] of fresh (spent)[c]	a (Å) of fresh (spent)[c]	S_{BET} (m^2/g) of fresh (spent)[c]	Pore volume (cm^3/g) (10^{-2}) of fresh (spent)
	Co	Cu	Fe				
0.0	—	27.1	46.2	15.25 (18.68)	8.3898 (8.4069)	28.8 (23.0)	5.1 (3.4)
0.25	6.1	20.2	46.7	13.85 (14.49)	8.4051 (8.4120)	34.0 (32.8)	6.7 (5.7)
0.50	12.4	13.5	47.1	13.17 (15.78)	8.4012 (8.4082)	43.8 (53.2)	10.9 (7.1)
0.75	18.6	6.9	47.3	14.77 (19.72)	8.3982 (8.4029)	36.6 (43.4)	6.4 (6.0)
1.0	25.1	—	47.6	14.13 (19.48)	8.3997 (8.4020)	36.8 (27.6)	5.9 (4.7)

[a] Chemical analysis results obtained from XRF spectroscopy.
[b] Obtained from Scherrer equation (Ref. (42)).
[c] Spent catalysts are after methylation reaction at 350°C for 10 h with 1 : 5 composition of PhOH : MeOH.

area of any element and the complex nature of active centers in these materials make it unsuitable to express the results in turnover frequency. Hence the results are given in mole percent.

3. RESULTS

3.1. Bulk Characterization (Chemical Analysis, XRD, and Surface Area)

Chemical compositions and structural and textural properties of $Cu_{1-x}Co_xFe_2O_4$ spinel system catalysts prepared in the present study are summarized in Table 1. XRF results display the bulk metal ion concentrations in line with the starting composition. Surface area decreases on spent catalysts due to carbon deposition compared to fresh catalysts; however at $x = 0.5$ and 0.75 an increase in surface area indicates segregation of active species on the surface. Figure 1 shows the XRD patterns of calcined (Fig. 1a) and spent (Fig. 1b) catalysts. It can be seen that the fresh Cu-rich catalyst ($x = 0.0$) exhibits a diffraction pattern attributed to the cubic spinel phase (39) and a considerable amount of the CuO and Fe_2O_3 phases. This indicates that the spinel formation is not completed at 500°C for $x = 0.0$, in agreement with literature reports (39–42). Substitution of Cu by Co increases the overall crystallinity of the spinel phase and all

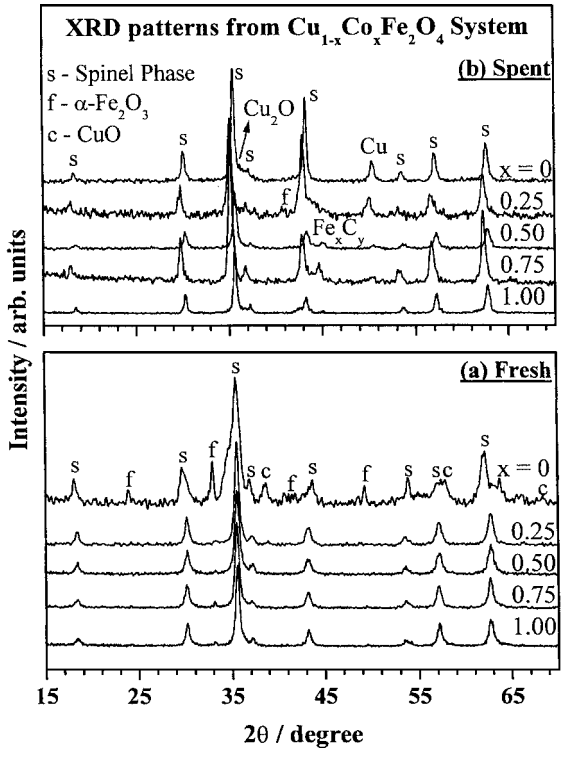

FIG. 1. X-ray diffractograms of fresh (a) and spent (b) $Cu_{1-x}Co_xFe_2O_4$ catalysts. XRD from spent catalysts are after phenol methylation reaction at 350°C for 10 h with 1 : 5 composition of phenol : methanol.

the peaks are indexed as reported on ASTM cards (cards 1-1121 and 3-0864). However, trace amounts of the α-Fe_2O_3 impurity phase were also detected with $x \geq 0.25$. The lattice constants, a, obtained for $CuFe_2O_4$ and $CoFe_2O_4$ are 8.3898 and 8.3997 Å, respectively, close to the literature value (39, 43, 44). The broad peaks seen in XRD indicates the fine particle size of the ferrite formed due to coprecipitation in contrast to the sharp peaks reported for materials prepared by ceramic method. It is also evident from the crystallite size of 13–16 nm for all samples (Table 1) estimated from the most intense peak (311) using the Scherrer equation (45),

$$D_{hkl} = 0.9\lambda / B \cos\theta, \qquad [1]$$

where D_{hkl}, λ, B, and θ are the volume-averaged particle diameter, X-ray wavelength, full width at half maximum (FWHM), and diffraction angle, respectively. The results are given in Table 1.

XRD analyses of spent catalysts, after reaction with a phenol : methanol (PhOH : MeOH) ratio of 1 : 5 at 350°C for 10 h, shown in Fig. 1b, were examined in a similar manner. At $x = 0.0$ few lines are observed in contrast to the same fresh catalyst and d values are the same in both cases. Some peaks disappear corresponding to CuO and α-Fe_2O_3; however, new peaks appear that match Cu and Cu_2O and their intensity decreases at higher x. Mössbauer analysis indicates small amounts of Fe_xC_y detected in some compositions (46); however, the original catalytic activity is regained after the spent catalyst is oxidized. These results indicate the reductive reaction condition. The spent catalysts are crystalline and all the peaks are indexed. No change in XRD pattern is observed for fresh and spent $CoFe_2O_4$. A small increase in a and a considerable enhancement in crystallite size are observed on spent catalysts.

3.2. Catalytic Methylation of Phenol

3.2.1. Effect of MeOH : PhOH molar ratio. Phenol methylation was carried out at 350°C on $x = 0.50$ using MeOH : PhOH molar ratios between 3 and 7 (Fig. 2, bottom) to obtain the optimum reactants composition for detailed studies; time dependence of phenol conversion for all catalyst compositions is also shown in Fig. 2 (top). Phenol conversion gradually increases with the above ratio and a maximum of 98 mol% conversion is achieved at ≥5. Selectivity of major products, *o*-cresol and 2,6-xylenol, show a linear dependence but in an opposite direction with increasing MeOH. Although conversion level is constant at ≥5, a marginal increase in selectivity of 2,6-xylenol was observed at high molar ratios. These facts revealed that 2,6-xylenol is produced at the expense of *o*-cresol. In addition a decrease in total ortho selectivity was observed at high MeOH : PhOH ratios (≥6) due to an increase in the formation of other methylated products, altogether reaching the level of 5.5 mol%. Excess methanol also causes more deactivation due to coking and it is confirmed from the large

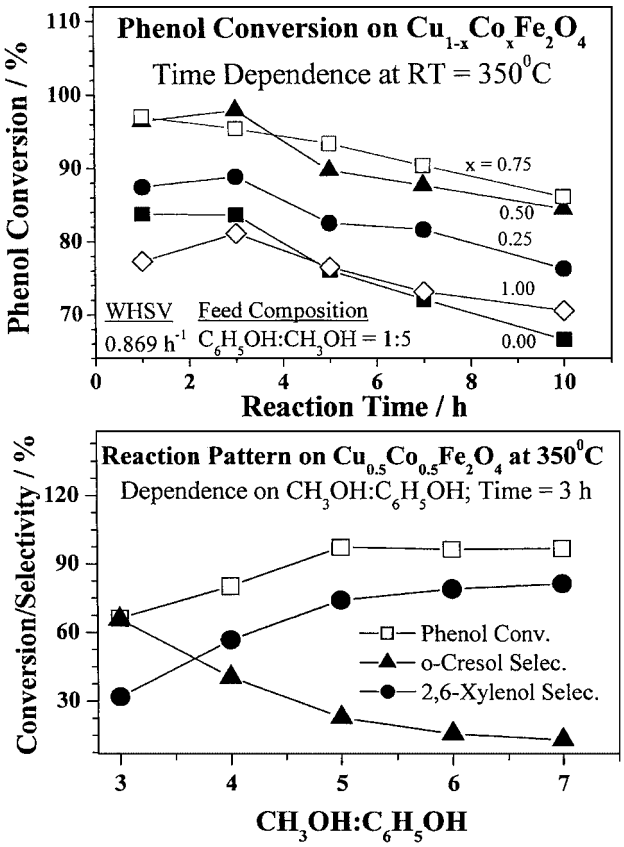

FIG. 2. (Top) Time dependence of phenol conversion on $Cu_{1-x}Co_xFe_2O_4$ catalysts at 350°C. (Bottom) Methanol : phenol composition dependence of phenol conversion and ortho product selectivity on $Cu_{0.5}Co_{0.5}Fe_2O_4$, $t = 3$ h at 350°C.

weight loss due to carbon burning in air in thermogravimetric analysis (data not shown). The above results demonstrate that the MeOH : PhOH ratio of 5 is preferred from the conversion, desired selectivity, and less-deactivation point of view. A similar trend was observed at $x = 0$ and 1, which suggests the MeOH : PhOH ratio was 5 : 1, irrespective of catalysts composition.

It is clear that excess methanol is necessary, even though reaction stoichiometry suggests a MeOH : PhOH ratio of 2 for 2,6-xylenol. Since the reaction is performed in vapor phase setup, some amount of methanol will be lost due to unavoidable side reactions, such as methanol reforming and simple gasification. The acidic nature of the catalyst might help prevent the above side reactions to some extent. In view of the above we studied the influence of water in the feed over an extended reaction period of time on a few compositions (results not shown). A PhOH : MeOH : H_2O ratio of 1 : 5 : 2 was used in this study. Generally, a prolonged stability is observed with considerably low deactivation compared to the feed without H_2O. Needless to say the advantage of H_2O in the feed is that the steam will suppress coke formation by a water–gas shift reaction and will maintain catalytic activity for a longer period. Detailed studies are in progress and will be reported elsewhere (47). Further, methylation carried out in H_2 atmosphere showed fast deactivation of the catalyst with low PhOH conversion, demonstrating that a large reduction of catalyst suppresses the methylation and hints at the possibility that the metallic species are not the methylation centers. In addition, test reactions were carried out with MeOH alone on ferrospinels. Product analysis displayed typical reformate products and after about 5 h methanol also started condensing. Thermogravimetric analysis of the above catalysts clearly indicates that the amount of coke is comparable to that of catalysts treated with a 1 : 5 ratio of PhOH : MeOH. This hints at the possibility that the coke formation is mostly due to MeOH decomposition and other routes, such as phenol–resin polymerization, are less likely under our experimental conditions.

Figure 2 (top) shows a decrease in phenol conversion, in general, with reaction time for any catalyst composition. Comparable high phenol conversion is observed at $x = 0.5$ and 0.75 and all other compositions show relatively lower conversion levels. Phenol methylation gave predominantly (≥97.5 mol%) *ortho* methylated products, viz., *o*-cresol and 2,6-xylenol, over $Cu_{1-x}Co_xFe_2O_4$ (Figs. 3 and 4). Minor products such as anisole, 2,4-xylenol, *p*-cresol, and 2,4,6-trimethyl phenol (TMP) were also produced altogether in the 0.5–2.5 mol% range (data not shown) irrespective of composition and temperature. However, at ≥375°C a slight increase in side products, up to 5 mol%, was observed. Detailed results are presented in the following.

3.2.2. Effect of catalyst composition. Figure 3 shows the selectivity of *o*-cresol (Fig. 3a), 2,6-xylenol (Fig. 3b),

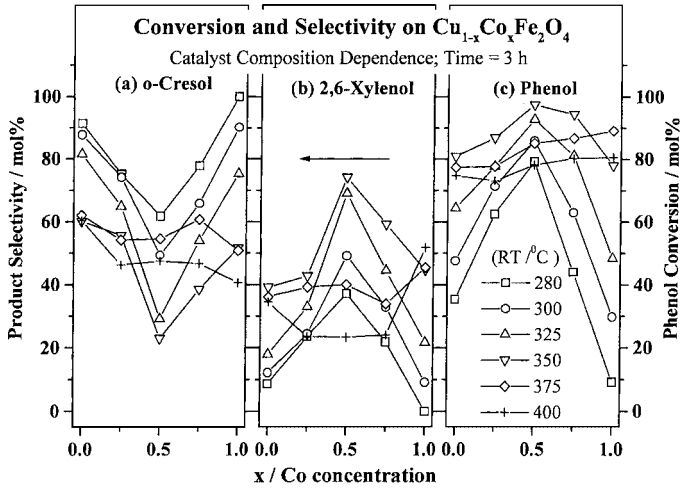

FIG. 3. Composition dependence of selectivity of *o*-cresol (a) and 2,6-xylenol (b) and phenol conversion (c) between 280 and 400°C on $Cu_{1-x}Co_xFe_2O_4$. Note that 2,6-xylenol selectivity increases at the expense of *o*-cresol, which indicates the sequential methylation.

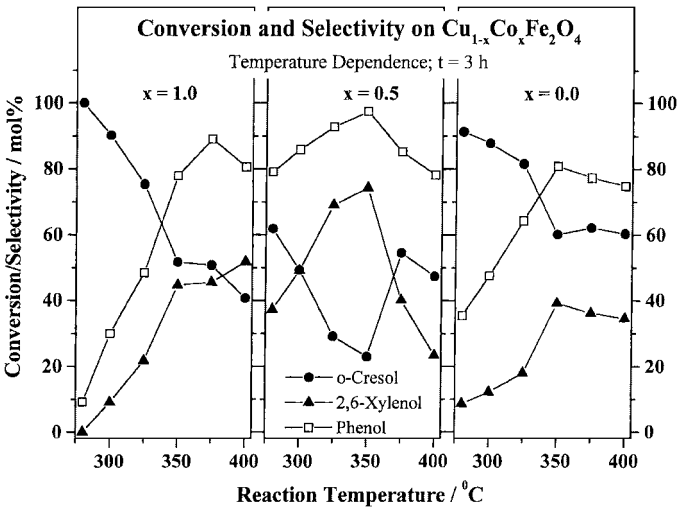

FIG. 4. Temperature dependence of phenol conversion and product selectivity for $x = 1.0$ (left), 0.5 (middle), and 0.0 (right). The linear increase in phenol conversion and 2,6-xylenol selectivity with increasing temperature indicates the first-order dependence of phenol conversion.

and phenol conversion (Fig. 3c) as a function of catalyst composition at different temperatures. The influence of the Cu–Co combination is a factor decisive to phenol conversion and 2,6-xylenol selectivity is evident from the following results: (i) phenol conversion increases from end compositions ($x = 0$ and 1) to intermediate compositions ($0 < x < 1$) up to 350°C and comparable conversion is observed at ≥375°C at all x values, though overall conversion decreases; (ii) the large selectivity of *o*-cresol found at $x = 0$ and 1 gradually changes toward 2,6-xylenol at $0 < x < 1$; (iii) 2,6-xylenol is produced at the expense of *o*-cresol; and (iv) a general decrease in phenol conversion and a change in the product selectivity pattern is observed at ≥375°C. The $x = 0.5$ composition displays large phenol conversion and selectivity toward 2,6-xylenol at 350°C, although other compositions, too, exhibit high conversion, ≥90 mol%, but not selectivity. This indicates that an equal amount of Cu and Co is necessary in the bulk for effective ortho dimethylation. A deviation from the above trend is observed at 400°C, with high 2,6-xylenol selectivity at end compositions and an increase in secondary product selectivity to >20 mol% at $0 < x < 1$.

3.2.3. Reaction temperature dependence. The effect of reaction temperature on phenol methylation is shown in Fig. 4 for $x = 0$, 0.5, and 1. These results were presented above but are displayed in a new way here to highlight the correlation between conversion and selectivity. Figure 4 demonstrates the following. (i) Phenol conversion increases linearly with temperature up to 350°C and a concurrent increase (decrease) in 2,6-xylenol (*o*-cresol) selectivity is observed at any given x. (ii) There is positive and negative first-order dependence on phenol conversion for 2,6-xylenol and *o*-cresol selectivity, respectively, for all compositions up to 350°C. (iii) The decrease in *o*-cresol production compensated for by an increase in 2,6-xylenol selectivity shows that methylation is sequential and that the methylation rate also increase with temperature up to 350°C. (iv) There is importance in the 1 : 1 ratio of the Cu : Co combination in $x = 0.5$ at 280°C, as shown by catalytic activity comparable to that of end compositions at $T \geq 350$°C.

3.3. XPS Analysis

3.3.1. Oxygen 1s core level. Atmospheric degradation of solids can be identified from C 1s and O 1s spectra before and after *in situ* cleaning (48, 49). Figure 5 displays the O 1s core level spectra recorded before and after *in situ* scraping for $Cu_{0.5}Co_{0.5}Fe_2O_4$. A shoulder is visible on unscraped surface at a binding energy (BE) around 532 eV; however, it disappears mostly after scraping in the vacuum chamber and a significant increase in O 1s intensity is also observed. The main peak becomes more symmetrical and does not shift after scraping, as observed at 530.2 eV, as in an unscraped surface. Carbonate species disappear completely after scraping in C 1s spectra (data not shown). A shoulder at 532 eV on unscraped surface is attributed to impurities such as OH^- and CO_3^{2-} species and the main peak is attributed to oxide ions in the spinel phase. Measurements after repeated *in situ* scraping did not change the small intensity of the high BE, which indicates that it is inherent from the catalyst surface. Obviously the energy difference

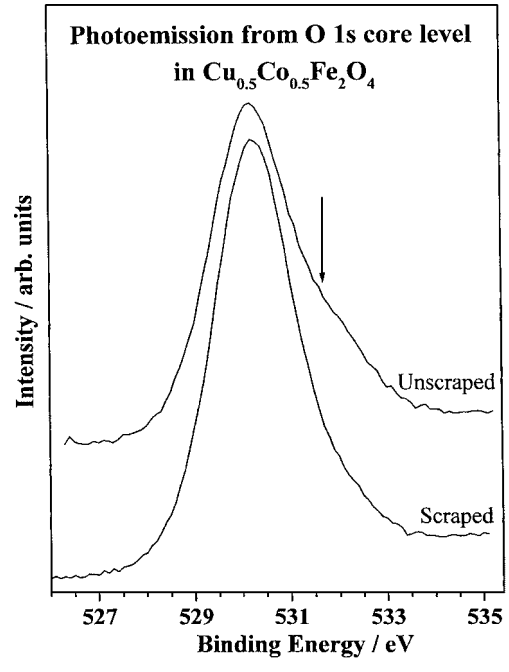

FIG. 5. O ls core level photoemission spectra from fresh $Cu_{0.5}Co_{0.5}Fe_2O_4$ catalyst obtained on as-received and *in situ* scraped surfaces. Note the large decrease in the shoulder intensity around 532 eV, indicated by the arrow, which demonstrates atmospheric degradation.

between oxygen species that are associated with Fe, Cu, and Co might be small and hence they overlap to a great extent and are difficult to resolve. No considerable difference is observed on the BE of the O 1s peak at different compositions. Similar contamination is observed on other fresh catalysts. XPS results on fresh catalysts in the following sections are taken after thorough scraping. However, spent catalysts are analyzed in the powder form as used in the reactions.

3.3.2. Cu 2p core level. The electronic structure of ferrospinels is investigated by XPS. Figure 6 presents the Cu 2p core level photoemission spectra from fresh or calcined (Fig. 6a) and spent (Fig. 6b) $Cu_{1-x}Co_xFe_2O_4$ catalysts. Spent catalysts are analyzed by XPS after methylation reaction at 350°C for 10 h with a 1 : 5 composition of PhOH : MeOH, unless otherwise stated. Relevant XPS results of the present system and standard compounds (50–53) are given in Table 2. It can be noticed that all fresh catalysts (Fig. 6a) exhibit the Cu $2p_{3/2}$ main peak at 934.2 ± 0.2 eV with a FWHM of 3.0 eV. Cu 2p BE does not change with Co content and indicates that the electron density on Cu remains the same. Good satellite intensity (I_s) is observed at all x values around 942 eV, indicating the existence of Cu^{2+} species. The intensity ratio between the satellite and the main line (I_s/I_m) is between 0.5 and 0.6 in all cases (inset to Fig. 6a), which is very close to that of pure CuO (50).

Cu $2p_{3/2}$ XPS results from spent catalysts are interesting and new features can be seen compared to fresh catalysts.

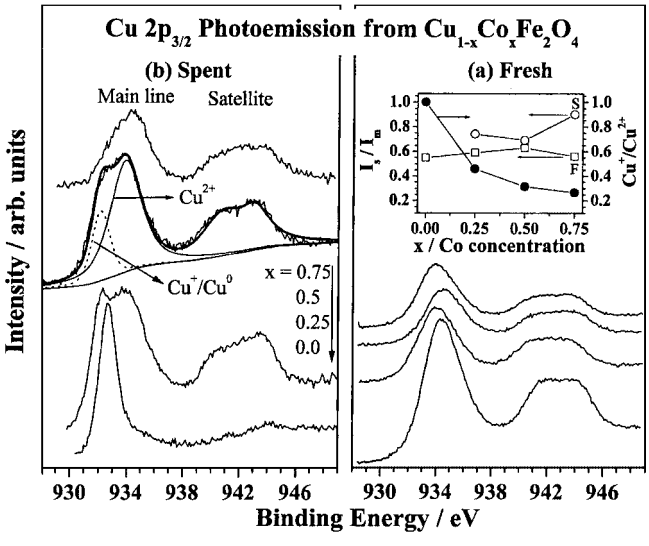

FIG. 6. Cu 2p photoemission spectra of fresh (a) and spent (b) $Cu_{1-x}Co_xFe_2O_4$ catalysts. Deconvolution clearly shows both Cu^+ (Cu^0) and Cu^{2+} on spent catalysts. (Inset) Satellite-to-main-line-intensity ratio I_s/I_m for fresh (F) and spent (S) catalysts (open symbols) and the ratio of Cu^+/Cu^{2+}, Cu reducibility, on spent catalysts (solid circle). Note the decrease in the reducibility of Cu with increasing x.

TABLE 2

XPS and XAES Parameters of $Cu_{1-x}Co_xFe_2O_4$ Catalysts and Relevant Reference Compounds

Compounds and x	BE of Cu $2p_{3/2}$ (FWHM) (eV)	KE of Cu–$L_3M_{45}M_{45}$ (eV)	α' (eV)	Reference
Cu	932.6	918.4	1851.0	51, 52
Cu_2O	932.5	916.5	1849.0	51, 52
CuO	933.8	917.6	1851.4	50
$Cu_{0.92}Fe_{2.08}O_4$	933.7, 935.7	NA	NA	53
0.00^F	934.3 (3.0)	917.2	1851.5	Present work
0.25^F	934.0 (2.9)	917.6	1851.6	Present work
0.50^F	934.4 (3.0)	917.8	1852.2	Present work
0.75^F	934.0 (3.0)	917.5	1851.5	Present work
0.00^S	932.6 (1.4)	916.4	1849.0	Present work
0.25^S	932.6, 934.3 (3.9)	917.0	1849.6, 1851.3	Present work
0.50^S	932.1, 933.9 (3.7)	917.3	1849.4, 1851.2	Present work
0.75^S	932.5, 934.3 (3.0)	916.9	1849.4, 1851.2	Present work

Note. F and S indicate fresh and spent catalysts.

At $x = 0.0$, a peak at 932.6 eV with a FWHM of 1.4 eV is observed without any satellite. However, at $x \geq 0.25$, there is a large broadening observed with a satellite feature at high BE. Deconvolution reveals the contribution of different species. For simplicity, it is shown only for $x = 0.5$ in Fig. 6b and the results are given in Table 2. Important points to be noted are the following: Cu species are reduced during reaction and the extent of reduction decreases with increasing Co content, and Cu^{2+} BE decreases by 0.4 eV at $x = 0.5$, with a concurrent decrease in I_s/I_m compared to other x values (inset to Fig. 6a). The above points clearly demonstrate that there is a strong influence from Co on Cu and its reducibility. The inset to Fig. 6a shows the I_s/I_m of fresh (F) and spent (S) catalysts and the reducibility of Cu. Reducibility of Cu, calculated as the amount of reduced Cu to Cu^{2+} content, decreases with increasing x. High polarizability induced by the formation of Co-containing Cu–spinel would change the nature of the Cu–O bond (54, 55).

3.3.3. Cu–$L_3M_{45}M_{45}$. Generally a modified Auger parameter (α') (50), calculated to distinguish the different oxidation (and final) states of Cu in the same or closely related compound, is defined as

$$\alpha' = h\nu + (\mathrm{KE\,Cu_{LMM}} - \mathrm{KE\,Cu\,2p_{3/2}}), \qquad [2]$$

where KE Cu_{LMM} and KE Cu $2p_{3/2}$ are kinetic energies of Auger electron and Cu $2p_{3/2}$ level, respectively. The Cu–$L_3M_{45}M_{45}$ Auger spectra of fresh and spent catalysts are shown in Figs. 7a and 7b, respectively. It can be seen that the $CuFe_2O_4$ exhibits the Cu–$L_3M_{45}M_{45}$ line at a KE of 917.2 eV. Co concentration increases the above value up to 917.8 eV. Note that for pure CuO this line appears at 917.6 eV (50). However, depending on the chemical

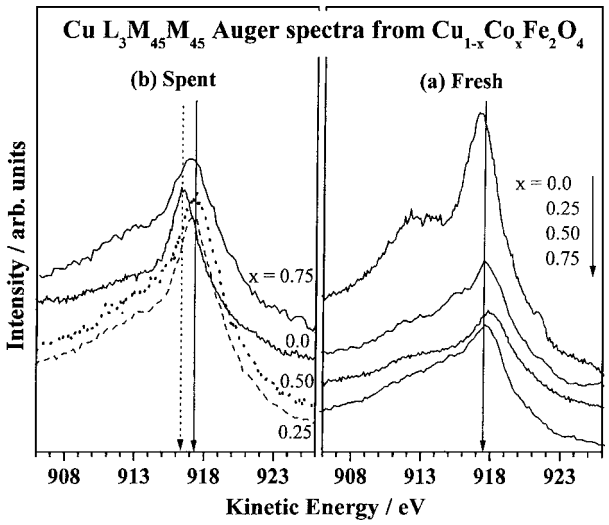

FIG. 7. X-ray-initiated Auger electron spectra (XAES) from Cu–$L_3M_{45}M_{45}$ fresh (a) and spent (b) $Cu_{1-x}Co_xFe_2O_4$ catalysts. Note the changes in shift and broadening of Auger transitions from spent catalysts. Spent catalyst spectra are normalized for better presentation.

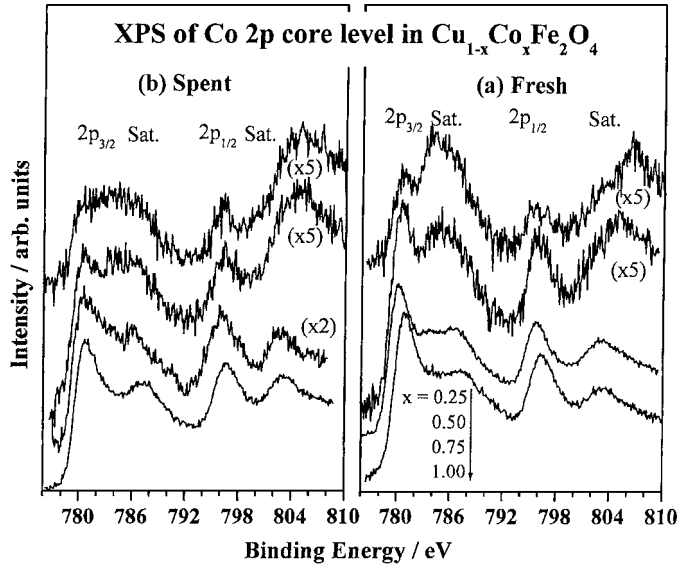

FIG. 8. Co 2p core level photoelectron spectra of fresh (a) and spent (b) $Cu_{1-x}Co_xFe_2O_4$ catalysts. Note an increase in the energy gap between spin orbit doublets of 2p levels and the decreasing satellite intensity with increasing x on fresh and spent catalysts.

environment and geometry, the position of this line has been found to shift significantly. α' determined (Table 2) in the 1851.5–1852.2 eV range, which is very close to that of CuO, has been obtained for fresh catalysts.

In contrast to fresh catalysts, spent catalysts show interesting observations in the Cu $L_3M_{45}M_{45}$ spectra (Fig. 7b), as in the Cu 2p core level. At $x = 0.0$, the above transition is observed with a relatively sharp peak at 916.4 eV, which is typical for Cu_2O. However, at $0.25 \le x \le 0.75$ a broad peak structure is exhibited at high KE, 917.5 eV. It is to be noted that the fresh catalysts also exhibit a single peak, around 917.5 ± 0.3 eV, in this region. This clearly indicates the increasing contribution of Cu^{2+} at higher x. However, the broadening indicates the contribution of Cu^+ species at low KE. At $x = 0.5$, an extra broadening seen on the high KE side at 918.6 eV indicates a Cu^0 contribution; $\alpha' = 1851.2$ eV also indicates the contribution of both Cu^0 and Cu^{2+} on $x = 0.5$ (see Table 2). Owing to a large overlap of the Auger transitions with a significant background in the spectra, a reliable estimation of individual Cu species is difficult. The above XPS and XAES of Cu suggest a distortion of the Cu^{2+} environment at intermediate compositions from fresh to spent catalysts.

3.3.4. Co 2p core level and Co–$L_3M_{45}M_{45}$ auger transitions. Co 2p photoemission spectra for fresh and spent catalysts are shown in Figs. 8a and 8b, respectively. It displays a main line and a satellite for Co 2p spin orbit doublets. XPS results are given with the reference compounds in Table 3 (56–58). Figure 8 and Table 3 show that (i) the I_s observed at a BE around 785 eV decreases with increasing x, (ii) the energy gap between Co 2p spin orbit doublets increases from 15 eV (15.5 eV) at $x = 0.25$ ($x \ge 0.5$) on fresh to 15.5 eV (16.0 eV) on spent catalysts, (iii) the energy gap between the main line and the satellite also increases with increasing x on both fresh and spent catalysts, and (iv) at $x = 0.75$ and 1, two satellites are discernible on the fresh catalyst from the large broadening, but only one satellite is seen on the spent catalyst (Table 3).

TABLE 3

XPS Parameters from Co 2p Core Level in $Cu_{1-x}Co_xFe_2O_4$ Catalysts and Relevant Reference Compounds

Material	BE of Co $2p_{3/2}$ (Satellite)[a] (eV)	Satellite intensity	$2p_{3/2}$–$2p_{1/2}$ gap (eV)	Reference
Co metal	778.0	—	15.1	56
CoO	780.1 ± 0.3	Strong	15.5	56–58
$Co(OH)_2$	780.9 ± 0.2	Strong	16.0	56–58
Co_2O_3	779.6	Weak	—	57
Co_3O_4	780.5	Weak	15.0	58
$ZnCo_2O_4$	780.3	Weak	15.0	58
$CoAl_2O_4$	781.9 ± 0.5	Strong	16	57, 58
$x = 0.25^F$	780.7 (4.0)	Strong	15.1	Present work
$x = 0.5^F$	780.5 (4.7)	Strong	15.5	Present work
$x = 0.75^F$	780.2 (3.4 and 6.1)	Intermediate	15.6	Present work
$x = 1.0^F$	780.9 (4.6 and 6.1)	Intermediate	15.5	Present work
$x = 0.25^S$	780.4 (4.1)	Strong	15.5	Present work
$x = 0.5^S$	780.5 (4.4)	Strong	15.9	Present work
$x = 0.75^S$	780.6 (4.5)	Intermediate	16.1	Present work
$x = 1.0^S$	780.7 (6.6)	Intermediate	16.0	Present work

Note. F and S indicate fresh and spent catalysts.

[a] Indicates the energy gap between Co $2p_{3/2}$ main line and satellite.

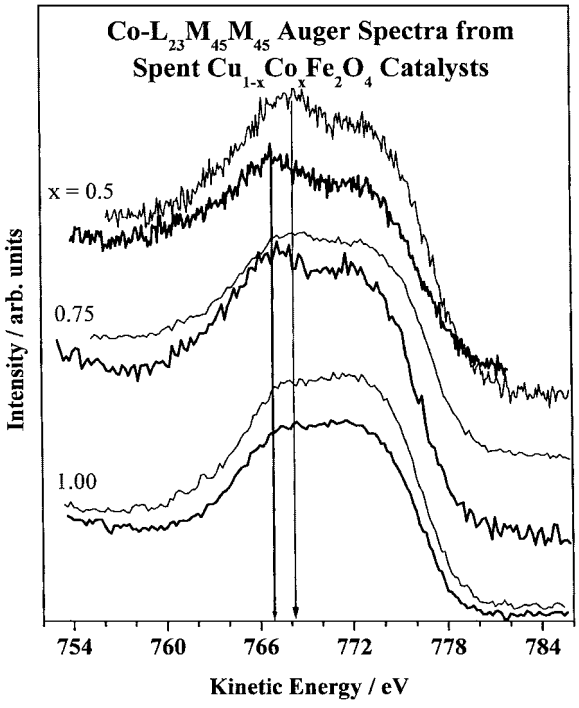

FIG. 9. XAES from Co–$L_3M_{45}M_{45}$ of fresh (thin lines) and spent (bold lines) $Cu_{1-x}Co_xFe_2O_4$ catalysts for $x = 0.5, 0.75$, and 1. Note the changes observed in energy and intensity at $x = 0.5$ and 0.75 from fresh to spent catalysts (thin and thick arrows, respectively).

A comparison of BEs of catalysts to those of reference compounds in Table 3 clearly indicates that the catalyst surfaces are in general composed of both Co^{2+} and Co^{3+}. High I_s for $x \leq 0.5$ suggests the contribution of Co^{2+} and high-spin Co^{3+}, since low-spin Co^{3+} shows poor I_s (56–58).

Co–$L_3M_{45}M_{45}$ Auger spectra of $x = 0.5, 0.75$, and 1 compositions, shown in Fig. 9, exhibit broad features between 760 and 780 eV. Two features, seen at 767 and 772 eV, are identical for fresh and spent catalysts at $x = 1.0$. However, at $x = 0.5$ and 0.75, a shift in energy is seen for the lower KE component on the spent catalyst compared to that of the fresh; further, a change in intensity ratio of the two features is observed. Significant changes on the spent catalyst at $x = 0.5$ and 0.75 imply that the final state of the low KE feature is different from that of other final state and indicate site-specific and/or near-neighbor interaction.

3.3.5. Fe 2p core level and Fe–$L_3M_{45}M_{45}$. Photoemission spectra from Fe 2p core levels normalized to $x = 0.0$ are displayed in Figs. 10a and 10b for fresh and spent $Cu_{1-x}Co_xFe_2O_4$ catalysts, respectively. It displays a main line and a satellite for both spin orbit doublets; a satellite associated with the $2p_{1/2}$ level is not shown, as there is some interference from O-KVV Auger transitions. Although at first glance the Fe 2p spectra look alike on fresh and spent catalysts, there are two important differences between them. (i) A clear satellite, due to predominant Fe^{3+}, is observed on the fresh catalysts; on the other hand, I_s is weak on the spent catalysts. (ii) The spent catalysts indicate a shoulder around 709.5 eV, characteristic of Fe^{2+} species (59, 60), which is shown after deconvolution in the inset in Fig. 10 for $x = 0.5$. This feature is observed at $0 < x < 1$ with a $Fe^{2+}:Fe^{3+}$ ratio of 1 : 2. Further, it is accompanied by a clear shift in the Fe $2p_{1/2}$ main peak to lower BE, 724.3 eV compared to 725 eV for $x = 0$ and 1 (Fig. 10b). It is to be emphasized here that Fe^{2+}–O bond length should be significantly different from that of Fe^{3+}–O and it influences Fe–O hybridization (60) and Cu or Co ions that are in the octahedral sites.

Figure 11 displays the Fe–$L_3M_{45}M_{45}$ spectra for $x = 0, 0.5$, and 0.75 catalysts. The spent catalyst spectrum is normalized to fresh for better presentation. Fresh catalysts are similar and no difference is observed. Significant changes are clear on the spent catalyst at $x = 0.5$ and 0.75. A shoulder seen at KE 697 eV (dotted arrow in Fig. 11) corresponds to Fe^{2+}; however, the intensity of this feature is less at $x = 0.75$. Although there is some line broadening on the spent catalyst at $x = 0.0$, it is not as considerable as for $x = 0.5$. Fe 2p and Fe–LMM results indicates the partial reduction of Fe^{3+} and that the extent of reduction might be small at $x = 0$ and 1 and high at $0 < x < 1$.

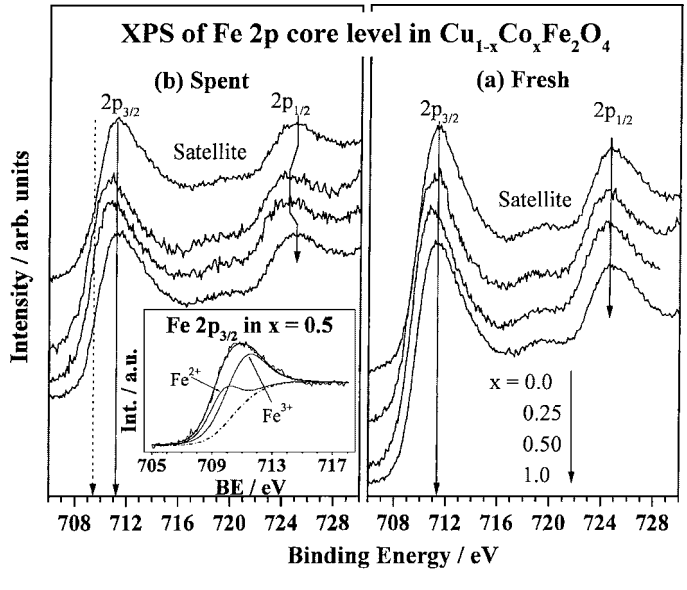

FIG. 10. Fe 2p core level XPS of fresh (a) and spent (b) $Cu_{1-x}Co_xFe_2O_4$ catalysts. A shoulder is seen below 710 eV on spent catalysts (dotted line) for $0 < x < 1$ with low satellite intensity. Deconvolution of the Fe $2p_{3/2}$ peak demonstrate Fe^{2+} and Fe^{3+} on spent catalyst at $x = 0.5$ (inset). The broadening and shift in BE is clear with the Fe $2p_{1/2}$ level (arrow).

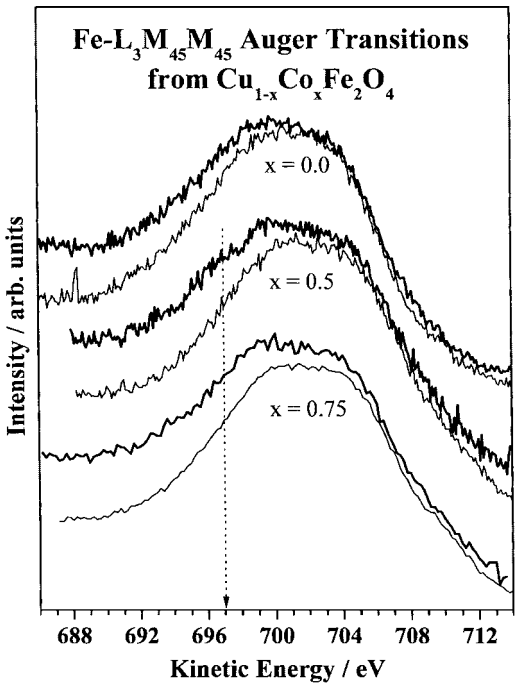

FIG. 11. XAES from Fe–$L_3M_{45}M_{45}$ of fresh (thin lines) and spent (bold lines) $Cu_{1-x}Co_xFe_2O_4$ catalysts for $x = 0.0$, 0.5, and 0.75 compositions. A shoulder observed at 697 eV on spent catalysts at $x = 0.5$ and 0.75 is indicated by the dotted line.

3.3.6. Valence band photoemission. XPS spectra of the valence band (VB) region obtained from fresh and spent $Cu_{1-x}Co_xFe_2O_4$ catalysts are shown in Figs. 12a and 12b, respectively. The main VB observed below 9 eV has contributions from 3d bands of Cu, Co, and Fe. At $h\nu = 1253.6$ eV, employed in these experiments, the photoionization cross-section (σ) value (Cu 3d = 0.021, Co 3d = 0.0067, Fe 2p = 0.0045, and O 2p = 0.0005 Mb) (61) is the dominating factor in formulating the spectral intensity. The above data suggest that Cu 3d should make large contributions to the VB and that contribution from O 2p is negligible. The VB assignments are straightforward from the intensity and the BE of the bands. High-intensity VB is observed with a satellite around 12 eV from the Cu $3d^8$ final state (62) on fresh $CuFe_2O_4$ and the intensity of the above features decreases at higher x, with an additional peak growing around 2 eV. Further, an overlapping band with significant intensity is discernible between 4 and 8 eV and it is clear on $CoFe_2O_4$. These observations demonstrate the position of the Cu and Co 3d bands, around 2 and 4 eV (solid and dotted lines), and the Fe 3d bands, between 4 and 8 eV. A dip in intensity between 3 and 4 eV denotes the absence of Cu 3d contributions at $x = 1$. The intensity variation observed from $x = 0$ to 1 is mostly due to the high σ of the Cu 3d bands.

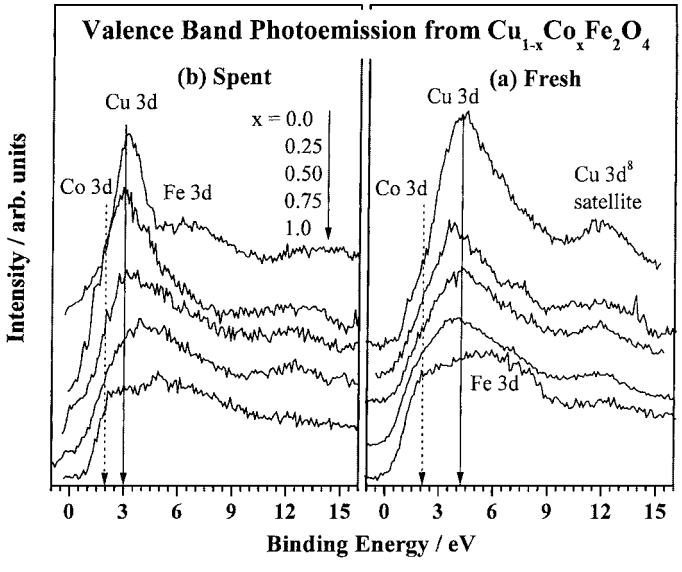

FIG. 12. Valence band XPS of fresh (a) and spent (b) $Cu_{1-x}Co_xFe_2O_4$ catalysts. A significant decrease in the energy gap between the 3d levels of Cu and Co and a decrease in the overall band width are observed on spent catalysts. Fe 3d level BE decreases on spent catalysts at $0.25 \le x \le 0.75$.

Dramatic changes observed on spent catalysts from core levels are reflected strongly in the VB spectra: (i) Cu 3d bands shift toward that of Co by $\geq$1 eV (arrows in Fig. 12b) accompanied by an enormous narrowing of the Cu 3d bands; (ii) the satellite disappears on $x = 0.0$, but a broad band (satellite) appears between 10 and 15 eV for $x = 0.25$–0.75; (iii) there is a clear shift in the onset of photoemission to 1 eV for $x = 1$ compared to emission from 0 eV on $x \le 0.5$; (iv) a shift in Fe 3d bands to lower BE at $0 < x < 1$ is discernible; and (v) Co 3d band remains at the same BE on fresh and spent catalysts. The above points demonstrate a large interaction among 3d bands of metal ions on spent catalysts compared to that of fresh catalysts. Finite photoemission at 0 eV also reflects the metallic conductivity, probably due to Cu^0, on $x \le 0.5$.

3.3.7. Bulk and surface composition. Bulk and surface composition values for all the catalysts are given in Tables 1 and 4, respectively. This exercise is mainly to understand the distribution of metals ions and their heterogeneity on the surface, as it directly influences catalytic activity. On fresh catalysts, there is a linear relation between the input amount (x) and bulk and surface concentrations measured by XRF and XPS, respectively. A high Cu/Fe ratio is found on spent catalysts at $0.25 \le x \le 0.75$. A good amount of C deposition is evident from Table 4; however, it is relatively less on $x = 0$ and 1. It is to be emphasized here that (i) the predominant Fe-enriched surface at $x = 0$ changes to a Cu + Co-enriched surface at $x = 0.25$ and 0.5 (Table 4) on spent catalysts, (ii) high coke content and low Co concentration is observed at $x = 0.25$ and 0.75, irrespective of bulk concentration, and (iii) (Cu + Co)/Fe varies in the small range of 1 ± 0.25 on fresh catalysts, but the variation is high on spent catalysts. The last point indicates an apparent support-like interaction of the Fe part of the catalyst, and

TABLE 4

Surface Atomic Ratio of Fresh and Spent $Cu_{1-x}Co_xFe_2O_4$ Catalysts

	Fresh			Spent			Spent		
x	Cu/Fe	Co/Fe	(Cu + Co)/Fe	Cu/Fe	Co/Fe	(Cu + Co)/Fe	Fe/C	Cu/C	Co/C
0.00	1.17	—	1.17	0.30	—	0.30	0.503	0.152	—
0.25	1.04	0.20	1.24	1.57	0.17	1.74	0.110	0.171	0.019
0.50	0.79	0.32	1.11	1.24	0.40	1.64	0.140	0.173	0.056
0.75	0.50	0.50	1.00	0.60	0.31	0.91	0.091	0.055	0.028
1.00	—	0.75	0.75	—	1.25	1.25	0.282	—	0.354

indicates the larger part of Cu and Co in the methylation reaction.

Figure 13 displays the Cu/(Co + Fe) (Co/Fe for $x = 1$) ratio calculated from XPS results in the left panel and phenol conversion with product selectivity for all compositions in the right panel. A correlation between them hints at the possibility that not a single ion but a combination of metal ions, specifically the heterogeneity of the surface, decides the course of the reaction toward high 2,6-xylenol selectivity. When the surface is dominated by a single metal ion ($x \leq 0.25$ and $x = 1$), desired reactivity is not achieved. Further, it is speculated here that it might be the pair of hetero-atoms, say Cu–Co or Cu–Fe, that is preferred for two different reactants to be adsorbed in nearby sites for the above desired selectivity and to avoid any diffusion. The same trend shown by both Cu/(Co + Fe) and (Cu + Co)/Fe for all x values supports the above points.

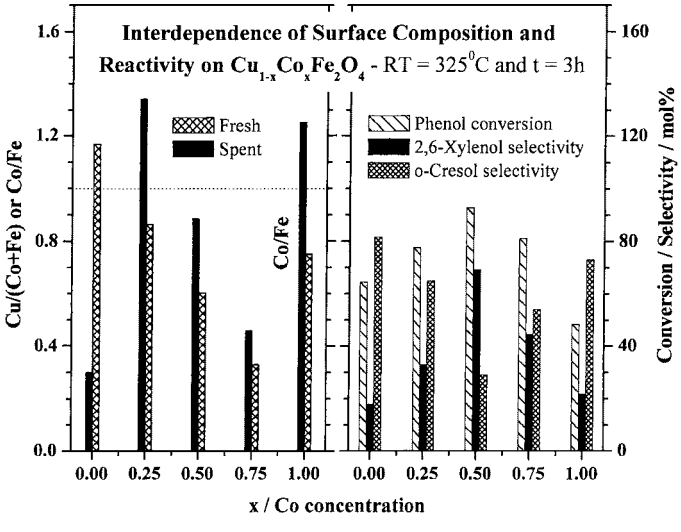

FIG. 13. Comparison of phenol conversion and *ortho* product selectivity performance of $Cu_{1-x}Co_xFe_2O_4$ catalysts at 325°C, $t = 3$ h (right) and atomic ratio of Cu/(Co + Fe) (or Co/Fe) for Cu-containing (Cu less) catalysts (left). Note the large production of desired 2,6-xylenol and Cu/(Co + Fe) = 0.9 at the $x = 0.5$ composition on the spent catalyst.

4. DISCUSSION

4.1. Catalytic Performance

An important aspect of the methylation reaction to the discussion presented here is related to the dependence of the product selectivity on phenol conversion. High phenol conversion (98 mol%) and 2,6-xylenol selectivity (75 mol%) is achieved at $x = 0.5$ composition between 325 and 350°C. However, moving either side of the above conditions, in terms of reaction temperature as well as catalyst composition, increases the selectivity of *o*-cresol while decreasing phenol conversion (Figs. 3 and 4). A linear relation is shown between increasing phenol conversion and 2,6-xylenol selectivity at temperatures up to 350°C in Fig. 4. Hence high phenol conversion becomes a prerequisite for dimethylation to produce 2,6-xylenol. However, this is not the case with *o*-cresol, as its selectivity declines with increasing phenol conversion. These two points actually suggest the stepwise methylation of PhOH to 2,6-xylenol through *o*-cresol at a high phenol conversion. Near total *ortho* product formation below 350°C at all x values indicates, in general, that the desoprtion of *ortho* products is high. At high MeOH : PhOH ratios (≥6) a high methylation capacity with low phenol on the catalyst surface leads to more secondary products. Time-dependent spectroscopy under reaction conditions will throw more light on this reaction pathway.

Low selectivity of 2,6-xylenol observed at $x = 0$ and 1 is attributed to a larger degree of gasification of MeOH than its decomposition. This is clearly supported by the low carbon content on the spent catalysts at $x = 0$ and 1 compositions (Table 4). The better selectivity of 2,6-xylenol and the high C content observed clearly suggest that methanol decomposition increases at $0 < x < 1$ (Figs. 3 and 4). This is further clear from the very high 2,6-xylenol selectivity (≥80 mol%) observed at $x = 0.5$ with high MeOH : PhOH ratios of 6 and 7 (Fig. 2). Mixed metal oxides of CuO–Fe_2O_3 and CoO–Fe_2O_3 show about 68% methanol gasification (15, 16) at 350°C, supporting our findings about the necessity of high methanol in this reaction on ferrospinels. Although $x = 0$

and 1 shows decreasing phenol conversion at $T > 375°C$, an increase in 2,6-xylenol selectivity indicates an increase in methanol decomposition and dimethylation capacity.

Introduction of Co into the $CuFe_2O_4$ system (at $x = 0.25$) shows an increase in phenol conversion, to 62 mol% from 35 mol% at $x = 0.0$ at 280°C (Fig. 3). In contrast, introduction of Cu into $CoFe_2O_4$ ($x = 0.75$) displays a fivefold increase in phenol conversion and an increase in 2,6-xylenol selectivity to 22% from no 2,6-xylenol at 280°C. Further, high phenol conversion achieved at 350°C at $x = 0.75$ is 94 mol%, whereas the same is 87% in the $x = 0.25$ case. This underscores the fact that the role of Cu is relatively higher than that of Co in phenol methylation.

General observation of reduced metal ions on the spent catalyst reveals that the overall reaction takes place under reduction conditions. It is obvious that methanol reformation is highly plausible, and the role of the present acidic catalyst is to suppress the above reaction. This is also a reason for a high level of methanol in the feed employed in methylation reactions. It is known that Cu and Co are good for H_2 production and hydrogenating the carbon species (32, 34–36), respectively. This fact supports the total reduction of Cu in $CuFe_2O_4$. In fact, in the CuCoZnCr oxide multicomponent system for methanol synthesis, a large amount of hydrocarbon has been noticed at high Co content (35, 63). Hydrogenation of CO and C species by Co is an advantage to the present reaction, as it reduces the C content, enhances methylation, and hence lengthens the active lifetime of the catalysts. Figure 2 clearly shows the slow deactivation of $x = 0.5$ and 0.75 compositions and a phenol conversion of 85% is observed even at $t = 10$ h. High 2,6-xylenol selectivity with relatively low amounts of C deposition at $x = 0.5$ compared to that at $x = 0.25$ clearly indicates that the hydrogenation of carbon species occurs as a secondary process. Fe-enriched surfaces at $x = 0.0$ (spent) and 1.0 (fresh) show fast deactivation (Fig. 2) and low 2,6-xylenol selectivity indicates that the role of Fe is not high in methylation. These facts reinforce our earlier conclusions that a heterogeneous surface enhances the desired selectivity, as shown in Fig. 13.

4.2. Chemical State and Distribution of Transition Metal Ions in the $Cu_{1-x}Co_xFe_2O_4$ System

Spent catalysts show predominant spinel phase and small amounts of metallic Cu, iron carbide, and Cu_2O due to a reductive atmosphere under methylation conditions. Nonetheless Cu^0 and Fe^0 are not observed in XPS results (Fig. 6 and 10) at any composition, hinting at the possibility the surface metal atoms are oxidized. However, coke deposition prevents the oxidation of metal species in the bulk and seen in XRD. This also indicates the inevitable structural collapse to some extent at $x = 0.0$; nevertheless, the structural integrity retained is high at $x \geq 0.25$ and is confirmed from XRD. Surface area increases after reaction on $x = 0.5$ and 0.75 and the same decreases at other compositions. At $x = 0.0$ and 0.25 it is probably due to agglomeration of Fe and Cu particles, respectively (Fig. 13). Nonetheless, $x = 0.5$ shows uniform distribution of all the ions, and copper, being the major species, supports its high activity. All the above indicate there is a considerable redistribution of the cations under reaction conditions, especially at $0 < x < 1$. Seemingly, there is an apparent correlation between surface area and phenol conversion. It is to be noted here that the surface area of the $Cu_{1-x}Co_xFe_2O_4$ system prepared by a high-temperature glycine nitrate combustion method (64) exhibits <2 m^2/g for all compositions and shows low methylation activity (results not shown) but follows the same trend as that of samples prepared by coprecipitation. This indicates that the surface area is not a dominating factor in methylation reactions.

A number of changes observed between fresh and spent catalysts throw more light on the transformations that occur under experimental conditions. The main points from the XPS results can be summarized in a nutshell: a decrease in the reducibility of copper with increasing x, increasing 3d band overlap and redistributing metal ions on spent catalysts. There is no static charging observed on any of the spent catalysts and a weak photoemission at 0.0 BE, except at $x = 1$, demonstrates the bulk conducting nature of the catalysts, in agreement with XRD results. The main observations from XPS in combination with the desired reaction pattern at $x = 0.5$ suggest that the metal ions should be distributed optimally to have a large 3d band overlap. These factors demonstrate a hand-in-hand change, enhance the heterogeneity of the surface chemically, and integrate the material electronically in such a way that multireactions are carried out in close proximity. This also indicates the synergism and effective utilization of reactants in this ferrospinel catalyst at $0 < x < 1$. Large production of 2,6-xylenol with high phenol conversion and a ratio of 0.9 for $Cu/Co + Fe$ at $x = 0.5$ requires the optimum distribution of active species to have a highly heterogeneous surface.

4.3. Cu–Co Synergism

XPS results in the present study clearly indicate that the Cu and Co 3d bands and their overlap play a central role in the catalytic performance in the methylation reaction. Cu-rich composition ($x = 0.0$) exhibits the total reduction of Cu species and the low-surface Cu atomic percent is possibly due to significantly large CH_3OH reforming and H_2 production. In contrast, at $x = 1.0$, no significant chemical changes are observed with Co in XPS. However, at intermediate compositions CH_3OH reforming is suppressed to a considerable level, as is also evident from the enhancement in the total amount of Cu species on the surface, Cu^{2+} content, and methylation activity compared to that when $x = 0.0$ (Fig. 13). The decreasing amount of reduced Cu species with increasing x is attributed to the participation

of Co in the hydrogenation activity under the present experimental conditions. Hydrogenation by Co consumes a considerable amount of H_2 and converts C and CO into methane, methyl, and MeOH species (33–35, 65, 66), which are utilized again through the normal methylation route. This is in addition to Co activating MeOH for methylation. The above process might be preferred in the presence of Co rather than the reduction of Cu^{2+} to Cu, as in $x = 0.0$.

Low phenol conversion and 2,6-xylenol selectivity at $x = 1$ change very significantly and favorably with the addition of Cu at $x = 0.75$ and 0.5, clearly demonstrating the prime importance of Cu in phenol adsorption and the combined effect of Cu + Co in 2,6-xylenol selectivity in this system, as discussed in the previous paragraphs. It is the latter factor, known as Cu–Co synergism, that plays a major role in the phenol methylation reaction, which is clearly evident from the above discussions. In the fresh catalysts the Co 3d band is the top-most energy level. Observation of metallic copper on the spent catalysts clearly hints at the possibility that the broad Cu 4s band (67) also overlaps with 3d bands of Cu, Co, and Fe at intermediate compositions under experimental conditions and makes these materials integrated chemically and electronically.

Recently we have shown that the Cu–Co mixed oxide hydrotalcite catalyst performs oxidative steam reforming (32) with a high rate of H_2 production and low levels of Co through a hydrogen spillover mechanism, as on Cu–ZrO_2 (68); XPS results also demonstrate a similarity between fresh and reduced catalysts. The above results support the idea that the Cu–Co synergism in the present ferrospinel environment also performs methanol reforming to produce H_2 as well as in hydrogenation of carbon species under methylation. The observed shift in the Fe 3d levels also suggests that Fe is not a silent spectator and is involved in the electronic structure of the catalyst, at least at all intermediate compositions. A change in the spin state of Co is also speculated to occur from fresh to spent catalysts by virtue of the change in energy gap between Co 2p spin orbit doublets and I_s (38) along with redistribution of Co in T_d and O_h sites (Figs. 8 and 9). At $x = 0.5$ the above changes are accompanied by changes in Cu and Fe photoemission too and support the idea that the spin state also can influence conversion and selectivity. IR studies on the above catalysts for acid–base properties support the above conclusions and a good correlation is observed with catalytic activity (69).

5. CONCLUSIONS

This paper reports the results from the catalytic and kinetic study of phenol methylation on $Cu_{1-x}Co_xFe_2O_4$ ferrospinel over a wide range of temperatures and catalyst composition with a reactant composition of phenol : methanol of 1 : 5. Fresh and spent catalysts were subjected to detailed analysis by XRD, XPS, and XAES. Analysis of the kinetic data hints at the possibility that under most reaction conditions the rate of the overall process might be limited by the first methylation step to *o*-cresol. At all x values phenol conversion increases with temperature at least up to 350°C, and there is a linear relation between conversion and 2,6-xylenol selectivity, which indicates the first-order conversion dependence. Total *ortho* selectivity is found at all catalyst compositions up to 375°C and 2,6-xylenol production is high at 350°C except for $CoFe_2O_4$. Large *o*-cresol selectivity decreases from end compositions to a minimum at $x = 0.5$ and a concurrent increase in 2,6-xylenol selectivity demonstrates that the mode of phenol methylation is sequential. It is inferred from the absence of *meta* and *para* products that the conversion of *o*-cresol to 2,6-xylenol is a relatively fast reaction. Copper species are active for methylation and cobalt catalyzes the hydrogenation of carbon species and decreases the coke content.

XRD, XPS, and XAES investigations on fresh catalysts clearly indicate the existence of Cu^{2+}, Fe^{3+}, Co^{2+}, and Co^{3+} species. However, the spent catalysts show composition-dependent oxidation states. A complete reduction of Cu^{2+} to Cu and Co^{2+}/Co^{3+} to Co^{2+} is observed at $x = 0.0$ and 1.0, respectively. At intermediate compositions, the reducibility of Cu decreases with increasing x and a partial reduction of Fe^{3+} to Fe^{2+} and a decrease in the BE of Fe 3d levels is observed. The valence band shows a change from marginal overlap between 3d bands of Cu and Co on fresh catalysts to a large overlap on spent catalysts. The Cu–Co synergism observed in ferrospinels is supported by the results from valence band, core levels, and kinetic results of desired selectivity at $x = 0.5$. The above observations also indicate the redistribution of cations on the spinel surface during the methylation reaction. The changes observed in the VB region on spent catalysts at intermediate compositions offer a picture on the overlap of 3d bands of all metal ions and with Cu 4s. The Co 3d level bridges the energy gap between 4s and 3d bands of Cu and this point underscores the role of Cu–Co synergism. These results confirm the existence of a strong interaction between transition metals in these materials and make it both chemically and electronically integrated.

ACKNOWLEDGMENTS

We thank one of the reviewers (Referee 1) for helpful suggestions. T.M. and N.R.S. thank CSIR, New Delhi, for a senior research fellowship.

REFERENCES

1. Oh, S. H., and Sinkevitch, R. M., *J. Catal.* **142**, 254 (1993).
2. Harold, H. K., and Mayfair, C. K., *Adv. Catal.* **33**, 159 (1985).
3. Warner, G. L., U.S. Patent 4,933,509 (1990) to General Electric Co., USA.
4. Battista, R. A., Bennett, J. G., Jr., Kokoszka, J. J., and Tungate, F. L., U.S. Patent 4,661,638 (1987) to General Electric Co., USA.

5. Tanabe, K., Hattori, H., Sumiyoshi, T., Tamaru, K., and Kondo, T., *J. Catal.* **53**, 1 (1978).
6. Bezouhanova, C., and Al-Zihari, M. A., *Appl. Catal.* **83**, 45 (1972).
7. Pierantozzi, R., and Nordquist, A. F., *Appl. Catal.* **21**, 263 (1986).
8. Belitrame, P., Belitrame, P. L., Carniti, P., Castelli, A., and Forni, L., *Appl. Catal.* **29**, 327 (1987).
9. Santacesaria, E., Grasso, D., and Carra, S., *Appl. Catal.* **64**, 83 (1990).
10. Santacesaria, E., Discrio, M., Ciambelli, P., Gelosa, D., and Carra, S., *Appl. Catal.* **64**, 101 (1990).
11. Balsama, S., Beltrame, P., Beltrame, P. L., Carniti, P., Forni, L., and Zureti, G., *Appl. Catal.* **13**, 161 (1984).
12. Velu, S., and Swamy, C. S., *Appl. Catal. A* **119**, 241 (1994).
13. Velu, S., and Swamy, C. S., *Appl. Catal. A* **145**, 141 (1996).
14. Sato, S., Koizumi, K., and Nozaki, F., *J. Catal.* **178**, 264 (1998).
15. Kotanigawa, T., Yamamoto, M., Shimokawa, K., and Yoshida, Y., *Bull. Chem. Soc. Jpn.* **44**, 1961 (1971).
16. Kotanigawa, T., and Shimokawa, K., *Bull. Chem. Soc. Jpn.* **47**, 1535 (1974).
17. Grabowska, H., Kaczmarczyk, W., and Wrzyszcz, J., *Appl. Catal.* **47**, 351 (1989).
18. Misono, M., and Nojiri, N., *Appl. Catal.* **64**, 1 (1990).
19. Narayanan, S., Venkatrao, V., and Durgakumari, V., *J. Mol. Catal.* **52**, L29 (1989).
20. Venkatrao, V., Durgakumari, V., and Narayanan, S., *Appl. Catal.* **49**, 165 (1989).
21. Venkatrao, V., Chary, K. V. R., Durgakumari, V., and Narayanan, S., *Appl. Catal.* **61**, 89 (1990).
22. Schwab, G. M., Roth, E., Grinzoz, C. H., and Mavrakis, N., *in* "Structure and Properties of Solid Surfaces" (R. Gomer and C. S. Smith, Eds.), p. 82. P. O. Univ. Chicago Press, Chicago, 1953.
23. Schwab, G. M., and Kraut, A. Z., *Anorg. Allgem. Chem.* **295**, 36 (1958).
24. Suchet, J. P., "Chemical Physics of Semiconductors." Van Nostrand, London, 1965.
25. Miller, A., *J. Appl. Phys.* **30**, 245 (1959).
26. Sreekumar, K., Mathew, T., Rajagopal, R., Vetrivel, R., and Rao, B. S., *Catal. Lett.* **65**, 99 (2000).
27. Sreekumar, K., Mathew, T., Mirajkar, S. P., Sugunan, S., and Rao, B. S., *Appl. Catal.* **201**, L1 (2000).
28. Sreekumar, K., Mathew, T., Devassy, B. M., Rajagopal, R., Vetrivel, R., and Rao, B. S., *Appl. Catal. A* **205**, 11 (2001).
29. Rao, B. S., Mathew, T., Shiju, N. R., and Vetrivel, R., Indian Patent pending.
30. Rao, B. S., Sreekumar, K., and Jyothi, T. M., Indian Patent 2707/98 (1998).
31. Narasimhan, C. S., and Swamy, C. S., *Appl. Catal.* **2**, 315 (1982).
32. Velu, S., Gopinath, C. S., and Suzuki, K., *J. Phys. Chem. B*, submitted.
33. Fierro, G., Jacono, M. L., Inversi, M., Dragone, R., and Porta, P., *Top. Catal.* **10**, 39 (2000).
34. Marchi, A. J., Di Cosino, J. I., and Apesteguia, C. R., *Catal. Today* **15**, 383 (1992).
35. Fornasari, G., Huysser, A. D., Mintcher, L., Trifiro, F., and Vaccari, A., *J. Catal.* **135**, 386 (1992).
36. Baker, J. E., Burch, R., and Golunski, S. E., *Appl. Catal.* **53**, 279 (1989).
37. Dongare, M. K., Ramaswamy, V., Gopinath, C. S., Ramaswamy, A. V., Scheurell, S., Brueckner, M., and Kemnitz, E., *J. Catal.* **199**, 209 (2001).
38. Joly, V. L. J., Joy, P. A., Date, S. K., and Gopinath, C. S., *J. Phys. Condensed Matter* **13**, 649 (2001).
39. Prince, E., and Treuting, R. G., *Acta. Crystallogr.* **9**, 1025 (1956).
40. Mexmain, J., *Ann. Chim. Paris* **4**, 429 (1969).
41. Mexmain, J., *Ann. Chim. Paris* **6**, 297 (1971).
42. Yamaguchi, T., *Proc. Fac. Eng. Keiogijuku Univ.* **19**, 776 (1967).
43. Smit, J., and Wijn, H. P. J., *Adv. Electron. Electronphys.* **6**, 83 (1954).
44. Jonker, G. H., *J. Phys. Chem. Solids* **9**, 165 (1959).
45. Henry, N. F. M., Lipson, J., and Wooster, W. A., "The Interpretation of X-Ray Diffraction Photographs." Macmillan, London, 1951.
46. Lázár, K., Koppány, Z., Mathew, T., Megyeri, J., Samuel, V., Mirajkar, S. P., Rao, B. S., and Guczi, L., *Phys. Chem. Chem. Phys.* **4**, 3530 (2002).
47. Mathew, T., Shiju, N. R., Rao, B. S., and Gopinath, C. S., Manuscript in preparation.
48. Gopinath, C. S., Subramanian, S., Paranthaman, M., and Hermann, A. M., *Phys. Rev. B* **48**, 15999 (1993).
49. Gopinath, C. S., Subramanian, S., Prabhu, P. S., Rao, M. S. R., and Rao, G. V. S., *Physica C* **218**, 117 (1993).
50. Moretti, G., Fierro, G., Jacono, M. L., and Porta, P., *Surf. Interface Anal.* **14**, 325 (1989).
51. Poulston, S., Parlett, P. M., Stone, P., and Bowker, M., *Surf. Interface Anal.* **24**, 811 (1996).
52. Strohmeier, B. R., Leyden, B. E., Field, R. S., and Hercules, D. M., *J. Catal.* **94**, 514 (1985).
53. Brabers, V. A. M., *Mater. Res. Bull.* **18**, 861 (1983).
54. Okamoto, Y., Fukino, K., Imamaka, T., and Teranishi, S., *J. Phys. Chem.* **87**, 3740 (1983).
55. Van der Laan, G., Westra, C., Haas, C., and Sawatzky, G. A., *Phys. Rev. B* **23**, 4369 (1981).
56. Stranick, M. S., Houalla, M., and Hercules, D. M., *J. Catal.* **106**, 362 (1987).
57. McIntyre, N. S., and Cook, M. G., *Anal. Chem.* **47**, 2210 (1975).
58. Zsoldos, Z., and Guczi, L., *J. Phys. Chem.* **96**, 9393 (1992).
59. Mills, P., and Sullivan, J. L., *J. Phys. D* **16**, 723 (1983).
60. Fujii, T., de Groot, F. M. F., Sawatzky, G. A., Voogt, F. C., Hibma, T., and Okada, K., *Phys. Rev. B* **59**, 3195 (1999).
61. Yeh, J. J., and Lindau, I., *Atmos. Data Nucl. Data Tables* **32**, 1 (1985).
62. Tjeng, L. H., Chen, C. T., Ghijsen, J., Rudolf, P., and Sette, F., *Phys. Rev. Lett.* **67**, 501 (1991).
63. Fornasari, G., Gusi, S., Trifiro, F., and Vaccari, A., *Ind. Eng. Chem. Res.* **26**, 150 (1987).
64. Chick, L. A., Pederson, L. R., Maupin, G. D., Bates, J. L., Thomas, L. E., and Exarhos, G. J., *Mater. Lett.* **10**, 6 (1990).
65. Cabet, C., Roger, A. C., Kiennemann, A., Läkamp, S., and Pourrow, G., *J. Catal.* **173**, 64 (1998).
66. Iglesia, E., *Appl. Catal. A* **161**, 59 (1997), and references therein.
67. Dekker, A. J., "Solid State Physics." Prentice Hall, London, 1981.
68. Jung, K. D., and Bell, A. T., *J. Catal.* **193**, 207 (2000).
69. Mathew, T., Shiju, N. R., Tope, B. B., Hegde, S. G., Rao, B. S., and Gopinath, C. S., *Phys. Chem. Chem. Phys.*, doi:10.1039/b20422bf.